

1
2
3
4
5
6
7
8
9
10
11
12
13
14
15
16
17
18
19
20
21
22

REVISION 1

A high-pressure structural transition of norsethite-type BaFe(CO₃)₂: comparison with BaMg(CO₃)₂ and BaMn(CO₃)₂

Chengcheng He^{1,2}, Chaoshuai Zhao³, Jianjun Jiang¹, Pan Wang¹, Heping Li^{1*}

1 Key Laboratory of High-temperature and High-pressure Study of the Earth's
Interior, Institute of Geochemistry, Chinese Academy of Sciences, Guiyang, 550081,
China

2 University of Chinese Academy of Sciences, Beijing, 100049, China

3 Center for High Pressure Science and Technology Advanced Research, Beijing
100193, China

* Corresponding author: liheping@mail.gyig.ac.cn

23
24
25
26
27
28
29
30
31
32
33
34
35
36
37
38
39
40
41
42
43
44
45
46

Abstract

Investigations on the phase stability of the norsethite-type family ($\text{BaMg}(\text{CO}_3)_2$, $\text{BaMn}(\text{CO}_3)_2$, $\text{BaFe}(\text{CO}_3)_2$) under high-pressure conditions are of great significance for understanding the structure and metal cationic (Mg^{2+} , Fe^{2+} , Mn^{2+}) substitution mechanism in double divalent metal carbonates. The structural evolution and equation of state of $\text{BaFe}(\text{CO}_3)_2$ were studied firstly at high pressure up to ~ 7.3 GPa by synchrotron X-ray diffraction (XRD) in diamond anvil cell (DAC) in this study. $\text{BaFe}(\text{CO}_3)_2$ undergoes a reversible phase transition from $R\bar{3}m$ (α -phase) to $C2/c$ (γ -phase) space groups at ~ 3.0 GPa. The fitted elastic parameters are $V_0 = 377.79(2) \text{ \AA}^3$ and $K_0 = 40.3(7)$ GPa for α - $\text{BaFe}(\text{CO}_3)_2$, $V_0 = 483.24(5) \text{ \AA}^3$ and $K_0 = 91.2(24)$ GPa for γ - $\text{BaFe}(\text{CO}_3)_2$ using second-order Birch-Murnaghan equation of state (BM2-EoS). Besides, the vibrational properties and structural stability of complete norsethite-type minerals were also investigated firstly by Raman spectroscopy combined with DAC up to 11.1 GPa. Similar structural phase transitions occur in $\text{BaMg}(\text{CO}_3)_2$, $\text{BaFe}(\text{CO}_3)_2$, $\text{BaMn}(\text{CO}_3)_2$ at 2.2-2.6, 2.6-3.7, and 3.7-4.1 GPa, respectively. The onset phase transition pressures of the norsethite-type family are much lower than that of dolomite-type $\text{Ca}(\text{Mg,Fe,Mn})(\text{CO}_3)_2$ and calcite-type $(\text{Mg,Fe,Mn})\text{CO}_3$ carbonates. These results provide new insights into the divalent cation substitution effects on the stability and structural evolution of carbonates under high-pressure conditions.

Keywords: Norsethite-type minerals, synchrotron X-ray diffraction, Raman spectroscopy, phase transition, diamond anvil cell

47

Introduction

48 Norsethite ($\text{BaMg}(\text{CO}_3)_2$), which can be derived from dolomite ($\text{CaMg}(\text{CO}_3)_2$)
49 by exchanging Ca with Ba (Lindner et al. 2017), has been studied extensively in
50 recent years because of its rapid precipitation at ambient conditions compared with
51 dolomite and magnesite (MgCO_3) (Hood et al. 1974; Lippmann 1967, 1973; Böttcher
52 et al. 1997; Böttcher 2000; Schmidt et al. 2013; Pimentel and Pina 2014, 2016; Liu
53 and Li 2020). Moreover, as a typical double carbonate, the formation conditions and
54 the potential influence on the global carbon cycle are of great significance for the
55 carbonate geochemistry (Scheetz and White 1977; Effenberger and Zemann 1985;
56 Böttcher et al. 1997; Schmidt et al. 2013; Effenberger et al. 2014; Pippinger et al.
57 2014; Zhuravlev and Atuchin 2020). The end-member of the norsethite-type family
58 includes $\text{BaMg}(\text{CO}_3)_2$, $\text{BaMn}(\text{CO}_3)_2$, and $\text{BaFe}(\text{CO}_3)_2$ (Liang et al. 2021; Böttcher et
59 al. 2022). All of them are typical layer structures with octahedra (MO_6 , $\text{M} = \text{Mg}, \text{Fe},$
60 Mn) and polyhedra (BaO_{12}) located exactly one above the other, parallel to the [001]
61 direction and separated by triangular CO_3 groups (Böttcher et al. 1997, 2012; Böttcher
62 2000; Pippinger et al. 2014; Liang et al. 2019, 2021), as shown in Figure 1(a).

63 The natural samples of norsethite and Mn-bearing norsethite were found in
64 natural environments (e.g., Costanzo et al. 2006; Zidarov et al. 2009), and the Mg and
65 Mn end-members of norsethite ($\text{BaMg}(\text{CO}_3)_2$ and $\text{BaMn}(\text{CO}_3)_2$) were also
66 synthesized under high pressure-temperature (P - T) conditions (e.g., Böttcher et al.
67 2012; Lindner et al. 2017, 2018; Liang et al. 2019). However, ferroan norsethite (e.g.,
68 $\text{BaFe}(\text{CO}_3)_2$) was never reported until recently successfully synthesized at high P - T

69 conditions (Liang et al. 2021). Norsethite-type minerals serve as a crystal chemical
70 and geochemical analogue for the dolomite-type minerals, which are regarded as one
71 of the most prominent deep carbon carriers (Effenberger and Zemann 1985; Böttcher
72 2000; Binck et al. 2020; Liang et al. 2021). Although the stability of $\text{BaMg}(\text{CO}_3)_2$,
73 $\text{BaMn}(\text{CO}_3)_2$ under high P - T conditions were extensively studied using different
74 methods (e.g., XRD, Raman spectroscopy, density functional theory) (Scheetz and
75 White 1977; Effenberger and Zemann 1985; Böttcher et al. 1997; Schmidt et al. 2013;
76 Effenberger et al. 2014; Pippinger et al. 2014; Lindner et al. 2017; Liang et al. 2019;
77 Zhuravlev and Atuchin 2020), whereas the high-pressure behavior of $\text{BaFe}(\text{CO}_3)_2$ is
78 still unclear. Synchrotron XRD, combined with DAC is a well-known technique to *in*
79 *situ* measure the structural evolution under high-pressure conditions (Liu et al. 2016;
80 Fu et al. 2017), by which we can get some clues for possible existence conditions of
81 ferroan norsethite from its high-pressure stability.

82 Partial cation substitution in carbonates is very common in natural samples, and
83 the effects of substitution with various compositions and proportions on the physical
84 and chemical properties of carbonates were extensively studied (e.g., Reeder and
85 Dollase 1989; Lin et al. 2012; Palaich et al. 2015; Cerantola et al. 2017; Zhao et al.
86 2020; Gabitov et al. 2021). Mn^{2+} or Fe^{2+} cations can often be incorporated into the
87 crystal structures in double carbonates, such as kutnahorite, ankerite, and norsethite-
88 type $\text{BaMn}(\text{CO}_3)_2$ (Rividi et al. 2010; Efthimiopoulos et al. 2017; Wang et al. 2022).
89 Previous studies showed that, in the dolomite group, cation substitution of Mg^{2+} by
90 Mn^{2+} could significantly lower the onset pressure of the phase transition (Wang et al.

91 2022), but this phenomenon was not obvious in the partial substitution of Mg^{2+} by
92 Fe^{2+} (Mao et al. 2011; Merlini et al. 2012). So how about the influence of cation
93 substitution in the norsethite-type minerals? There is still no answer yet. Given
94 Raman spectroscopy has classically been used as a very effective and convenient tool
95 to make semiquantitative estimates of solid solutions (e.g., Rividi et al. 2010; Farsang
96 et al. 2018; Dong et al. 2019; Efthimiopoulos et al. 2019; Binck et al. 2020), which
97 could be used to further study the mechanisms of Mg^{2+} , Fe^{2+} , Mn^{2+} replacement in the
98 norsethite-type carbonates.

99 In this study, we firstly used *in situ* high-pressure XRD to characterize the
100 structural changes of $\text{BaFe}(\text{CO}_3)_2$, calculated the isothermal compressibility, and
101 compared it with other carbonate phases. Besides, the effects of metal cation radius on
102 the high-pressure phase transition, Raman shifts, and pressure-induced mode shifts in
103 the norsethite-type minerals were investigated by Raman spectroscopy. We also
104 presented the pressure dependence and mode Grüneisen parameters of Raman-active
105 bands for $\text{BaFe}(\text{CO}_3)_2$, $\text{BaMg}(\text{CO}_3)_2$, and $\text{BaMn}(\text{CO}_3)_2$. These results provide new
106 insights into the understanding of high-pressure behavior of the norsethite-type
107 minerals.

108

109 **Materials and Methods**

110 High-purity single-crystal of the norsethite-type minerals $\text{BaFe}(\text{CO}_3)_2$,
111 $\text{BaMg}(\text{CO}_3)_2$, and $\text{BaMn}(\text{CO}_3)_2$ samples were synthesized at 3 GPa and 973 K for 2-
112 12 h on a DS 6 × 600 t cubic anvil type apparatus. Norsethite-type crystals have a

113 trigonal space group of $R\bar{3}m$, and no superstructure reflection was observed in the X-
114 ray images. The lattice parameters were refined to be $a = 5.022(1) \text{ \AA}$, $c = 16.752(1) \text{ \AA}$,
115 and $V = 365.85(8) \text{ \AA}^3$ for $\text{BaMg}(\text{CO}_3)_2$; $a = 5.092(1) \text{ \AA}$, $c = 17.309(1) \text{ \AA}$, and $V =$
116 $388.69(8) \text{ \AA}^3$ for $\text{BaMn}(\text{CO}_3)_2$; $a = 5.062(1) \text{ \AA}$, $c = 17.027(1) \text{ \AA}$, and $V = 377.81(8) \text{ \AA}^3$
117 for $\text{BaFe}(\text{CO}_3)_2$ at ambient conditions (Liang et al. 2021). A more detailed synthetic
118 method and characterization of three samples can be referred to Liang et al (2019,
119 2021).

120 High-pressure experiments for both synchrotron XRD and Raman spectroscopy
121 were conducted by a symmetric type of DAC equipped with a pair of 400 μm culet-
122 size diamond anvils. A thickness of 250 μm rhenium gasket was pre-indented to ~ 60
123 μm , and a diameter of around 160 μm was drilled by a laser drilling machine as the
124 sample chamber. A volume ratio of 4:1 methanol and ethanol mixture was selected as
125 the pressure transmitting medium (PTM), which can provide a quasi-hydrostatic
126 condition up to approximately 10 GPa (Klotz et al. 2009). Several tiny ruby (Cr^{3+} -
127 doped $\alpha\text{-Al}_2\text{O}_3$) spheres in Raman and gold (Au) powder in XRD experiments were
128 loaded into the sample chamber for pressure calibration (Mao et al. 1986; Shen et al.
129 2020), respectively. The pressures and uncertainties were calculated by the measured
130 pressure sensor before and after data collection.

131 For high-pressure single-crystal Raman experiments, three double carbonates
132 with good crystal morphology were loaded together into one sample chamber. Raman
133 spectra were collected from 100 to 1200 cm^{-1} on a Renishaw 2000 micro-confocal
134 laser Raman spectrometer with a 2400 lines/mm diffraction grating in the Key
135 Laboratory of High-Temperature and High-Pressure Laboratory Institute of
136 Geochemistry, Chinese Academy of Sciences, Guiyang. The Raman spectrometer was
137 calibrated using a single-crystal silicon wafer at 520 cm^{-1} before experiments.

138 Samples were excited by an argon ion laser ($\lambda = 514.5$ nm) operated at 20 mW with a
139 focused laser spot of approximately 5 μm in diameter through an SLM Plan 50 \times
140 Olympus microscope objective, and a spectrometer with a liquid nitrogen-cooled
141 CCD detector was used to collect the Raman data. The accurate peak positions were
142 fitted by the *PeakFit* software.

143 For high-pressure synchrotron powder-crystal XRD experiments, dozens of
144 colorless and transparent single crystals of neutral $\text{BaFe}(\text{CO}_3)_2$ were picked out and
145 ground with ethanol in an agate mortar for approximately 2 h to obtain homogeneous
146 powder samples (Liang et al. 2021). To avoid powder scattering, powder samples
147 were pressed slightly by two opposing diamond anvils to form a dense disk thinner
148 than 20 μm . Subsequently, a small piece of dense sample was loaded into the DAC
149 sample chamber. High-pressure synchrotron XRD experiments were carried out at the
150 BL15U1 beamline of the Shanghai Synchrotron Radiation Facility (SSRF). The
151 incident synchrotron X-ray beam was monochromatized to a wavelength of 0.6199 \AA
152 with a focused laser spot of approximately $2 \times 3 \mu\text{m}^2$ area. The diffraction patterns of
153 the samples were collected by a MAR-165 charge-coupled device (CCD) detector.
154 The distance of the sample-to-detector and the geometrical parameters of the detector
155 were calibrated with cerium dioxide (CeO_2) powder. All 2-D diffraction patterns
156 collected were integrated into conventional 1-D diffraction patterns by the *Fit2D*
157 program as a function of 2θ (Hammersley et al. 1996). Diffraction data were collected
158 at high pressures up to 7.3 GPa with intervals of 0.3-0.9 GPa. Whole XRD patterns
159 were analyzed by the *GSAS* software package (Larson and Von Dreele 2000), and
160 unit-cell parameters were refined by the Le Bail method (Le Bail et al. 1988).

161

162

Results and Discussion

163 **Equation of state of BaFe(CO₃)₂ at high pressure**

164 The powder X-ray diffraction patterns of BaFe(CO₃)₂ with increasing pressure at
165 room temperature were shown in Figure 2 (a). All the XRD peaks of BaFe(CO₃)₂ shift
166 toward higher angles with increasing pressure below 2.8 GPa. Then the XRD patterns
167 change significantly at 2.8 GPa, accompanied by the occurrence of several new peaks
168 at ~8.5°, 9.1°, 14.3°, and 17° and the disappearance of peak at ~13°. These
169 characteristics represent the onset phase transition of BaFe(CO₃)₂. Finally, the whole
170 XRD peaks remain from 3.2 to 7.3 GPa.

171 The XRD patterns of BaFe(CO₃)₂ were analyzed by the Le Bail refinements
172 using the *GSAS* program. Below 2.8 GPa, the XRD patterns agree well with the phase
173 at ambient conditions (Liang et al. 2021), which yields a trigonal structure (space
174 group $R\bar{3}m$) (Figure 2 (b)). Similar to α -norsethite (α -BaMg(CO₃)₂) (Pippinger et al.
175 2014), the trigonal phase is referred to as α -BaFe(CO₃)₂ in the following paragraphs.
176 Above 3.2 GPa, the powder XRD patterns of the new phase are similar to γ -norsethite
177 (γ -BaMg(CO₃)₂) with all the diffraction peaks indexed to the γ -BaMg(CO₃)₂-type
178 structure, which yields a monoclinic structure (space group *C2/c*) (Pippinger et al.
179 2014). Two representative XRD patterns of α -BaFe(CO₃)₂ phase at 2.0 GPa and 300
180 K, and γ -BaFe(CO₃)₂ phase at 5.6 GPa and 300 K were exhibited in Figures 2 (b) and
181 (c), respectively. The refinement results show great agreement with experimental
182 values, which indicate the reliable structures of α - and γ -BaFe(CO₃)₂ phases. At 2.8
183 GPa, the existence of the characteristics of both α - and γ -BaFe(CO₃)₂ phases is
184 noteworthy, indicating the coexistence of these two phases, namely, the mixture of α
185 + γ -BaFe(CO₃)₂ phase.

186 The pressure-volume (*P-V*) profiles of BaFe(CO₃)₂ were shown in Figure 3. The
187 *P-V* profiles of α - and γ -BaFe(CO₃)₂ phases with the $R\bar{3}m$ and *C2/c* structures were

188 well fitted by a BM2-EoS using the *EoSFit7c* software within the uncertainty of
189 measurements (Birch 1947; Angel et al. 2014). The equation of BM-EoS was shown
190 as follows:

$$191 \quad P = (3/2)K_0[(V_0/V)^{7/3} - (V_0/V)^{5/3}] \times \{1 + (3/4)(K'_0 - 4)[(V_0/V)^{2/3} - 1]\} \quad (1)$$

192 where V_0 , V , K_0 , and K'_0 are the ambient-pressure unit-cell volume, high-pressure unit-
193 cell volume, isothermal bulk modulus, and its pressure derivative ($K'_0 = 4$) at ambient
194 conditions. The fitting parameters are: $V_0 = 377.79(2) \text{ \AA}^3$ and $K_0 = 40.3(7) \text{ GPa}$ for α -
195 $\text{BaFe}(\text{CO}_3)_2$, $V_0 = 483.24(5) \text{ \AA}^3$ and $K_0 = 91.2(24) \text{ GPa}$ for γ - $\text{BaFe}(\text{CO}_3)_2$. Compared
196 to the norsethite-type family $\text{BaMg}(\text{CO}_3)_2$, the K_0 of α - $\text{BaFe}(\text{CO}_3)_2$ is distinctly
197 smaller than that of α - $\text{BaMg}(\text{CO}_3)_2$ ($K_0 = 66.2 \text{ GPa}$) (Pippinger et al. 2014). Different
198 from the comparable K_0 values of dolomite-type carbonates, the K_0 values are 95(1),
199 92(1), and 85(6) for $\text{CaMg}(\text{CO}_3)_2$, $\text{CaMg}_{0.6}\text{Fe}_{0.4}(\text{CO}_3)_2$, and $\text{Ca}_{0.76}\text{Mn}_{1.24}(\text{CO}_3)_2$,
200 respectively ($K'_0 = 4$) (Merlini et al. 2017; Palaich et al. 2015). It may be attributed
201 to the existence of superlattice in α - $\text{BaMg}(\text{CO}_3)_2$, which greatly improves its
202 incompressibility (Helmersson et al. 1987; Pippinger et al. 2014; Dong et al. 2015).

203 The refined lattice parameters of $\text{BaFe}(\text{CO}_3)_2$ at various pressures were listed in
204 Table 1. Changes in the unit cell volumes and lattice parameters throughout our
205 pressure range were depicted in Figures 3-4. The length of the a - and b -axes
206 contracted by 0.03(1) \AA while the c -axis contracted gradually by 0.57(1) \AA up to
207 pressures near 2.0 GPa. Above 2.8 GPa, the length of c -axis decreased by about 32%
208 while that of a -axis increased by 72% (Figure 4), which results in the expansion of the
209 unit cell volume by about 30% (Figure 3). For better comparison, we transform the

210 parameter values of the α -phase to an equivalent monoclinic cell setting (Figure S1).
211 All lattice parameters and volume as a function of pressure clearly show
212 discontinuous evolution, which can be assigned to the structural phase transition from
213 α -phase to γ -phase. In addition, the compressibility of $\text{BaFe}(\text{CO}_3)_2$ becomes harder at
214 high pressure, showing a nearly doubled bulk modulus K_0 of γ - $\text{BaFe}(\text{CO}_3)_2$. The
215 calculated density of γ - $\text{BaFe}(\text{CO}_3)_2$ is also found to be higher than the original phase
216 at ambient conditions accompanied 2% higher. Such a hardened behavior under high-
217 pressure conditions is also found in other carbonates. The bulk moduli K_0 are 92-95
218 and 76-83 GPa for dolomite-I, -II phases, respectively (Merlini et al. 2017). The
219 values are 112 and 175 GPa for high- and low-spin states of siderite (Ming et al.
220 2011), 113 and 144 GPa for rhodochrosite MnCO_3 -I and -II phases, (Liu et al. 2016),
221 97 and 155 GPa for magnesite MgCO_3 -I, -II phases, respectively (Maeda et al. 2017).

222 The axial compressibility and normalized lattice constants of $\text{BaFe}(\text{CO}_3)_2$ as a
223 function of pressure at room temperature were shown in Figure 4 (d). For α -
224 $\text{BaFe}(\text{CO}_3)_2$, our fitted axial modules to a , b , and c are $K_{a0} = K_{b0} = 324(22)$ GPa and
225 $K_{c0} = 56(2)$ GPa, which indicate a remarkable compressional anisotropy with the
226 compressibility of the c -axis being almost six times softer than that of other axes. The
227 great compressional anisotropy can be attributed to the rigid unit of the CO_3 groups,
228 which is a coplanar arrangement and nearly parallel to the (0001) plane direction. As
229 shown in Figure 1, the coplanar carbonate groups are out-of-plane tilt under high-
230 pressure conditions (Pippinger et al. 2014), which result in the difference in the
231 symmetries of the two phases and the decrease in compressional anisotropy for γ -

232 BaFe(CO₃)₂ with $K_{a0} = 287(22)$ GPa, $K_{b0} = 504(72)$ GPa, and $K_{c0} = 207(16)$ GPa. The
233 β angle steadily increases under compression within the pressure range (Figure S1(d)).
234 The a -axis shows a softening behavior at high pressure, and the b - and c -axes show
235 the opposite behavior.

236

237 **Raman spectroscopy of the norsethite-type family (BaFe(CO₃)₂, BaMg(CO₃)₂,**
238 **BaMnCO₃)₂) at high pressure**

239 To better compare the high-pressure behaviors of BaFe(CO₃)₂, BaMg(CO₃)₂,
240 BaMn(CO₃)₂, Raman spectra were obtained up to 11.1 GPa on the crystals of the
241 complete norsethite-type family. The expansion of the vibration was obtained through
242 factor-group analysis for norsethite-type crystals (Scheetz and White 1977; Zhuravlev
243 and Atuchin 2020):

$$244 \quad \tau_{tot} = 3A_{1g}(R) + 2A_{1u} + A_{2g} + 5A_{2u}(IR) + 4E_g(R) + 6E_u(IR) \quad (2)$$

245 There are 7 Raman-active modes, which contain internal vibrations of the carbonate
246 group and external lattice modes. The vibrations of the carbonate group (~700 to 1450
247 cm⁻¹) include fundamental symmetric and antisymmetric stretching (ν_1 , ν_3), out-of-
248 plane bending (ν_2) and in-plane bending (ν_4), among which ν_1 is the strongest
249 characteristic peak. In addition, the external lattice modes (< 400 cm⁻¹), derived
250 mainly from the translational lattice mode T and librational lattice mode L , could also
251 be obtained (Gillet et al. 1993). Similar Raman spectra of the norsethite-type family
252 were observed in the wavenumber range from 100 to 1200 cm⁻¹ at ambient conditions
253 (Figures 5, S2, S4). A weak peak (ν_2) can be observed in the Raman spectrum of
254 BaMg(CO₃)₂ at 880 cm⁻¹, which is not found in BaMn(CO₃)₂ and BaFe(CO₃)₂. The ν_2
255 internal mode belongs to the infrared-active mode, and chemical substitution affects
256 its activity. Such a phenomenon could also be observed in the dolomite system (Gillet

257 et al. 1993; Gunasekaran et al. 2006). Compared with previous studies of related
258 Raman-active modes for the norsethite-type family, the slight differences in
259 wavenumber for observed modes are due to the weak intensity, peak overlap,
260 orientation dependence, and synthetic environment (Scheetz and White 1977; Schmidt
261 et al. 2013; Liang et al. 2019; 2021).

262 The high-pressure Raman spectra of single-crystal of $\text{BaFe}(\text{CO}_3)_2$ were collected
263 in the diamond window of 100-1200 cm^{-1} at ambient temperatures. The pressure
264 dependence of the Raman spectra and shifts of $\text{BaFe}(\text{CO}_3)_2$ modes were shown in
265 Figures 5 and 6. Obviously, with increasing pressure, all the Raman bands of
266 $\text{BaFe}(\text{CO}_3)_2$ show blue shifts due to the decrease of corresponding bond length
267 (Ba/Fe/C-O) caused by crystal shrinkage. When the pressures of $\text{BaFe}(\text{CO}_3)_2$ up to 2.6
268 GPa, the ν_4 mode splits into two individual components, then with further
269 compression, T and L modes begin to split into two and three peaks, respectively, and
270 no new peak occurs after 3.7 GPa. Meanwhile, the pressure-induced frequency shifts
271 for the measurable modes all show a discontinuous evolution at 2.6 GPa, a transition
272 area at 2.6 to 3.7 GPa, and a stable linear relation with pressure after 3.7 GPa.
273 Referring to the XRD results of $\text{BaFe}(\text{CO}_3)_2$ in this study, both of these significant
274 changes could be attributed to the occurrence of structural phase transition from α -
275 $\text{BaFe}(\text{CO}_3)_2$ to γ - $\text{BaFe}(\text{CO}_3)_2$. Combined the high-pressure results of XRD and
276 Raman spectra, the more accurate phase transition range of $\text{BaFe}(\text{CO}_3)_2$ from α -phase
277 to γ -phase should be 2.6 to 3.2 GPa, and α -phase and γ -phase coexist in this pressure
278 range. XRD results reveal that the CO_3 groups are out-of-plane tile at high pressure,
279 which results in the vibrational environment change. So the T mode splits into three
280 peaks (T' , T'' , T'''), and the pressure coefficient ($\partial\nu_i/\partial P$) changes from 2.03(11) to
281 1.89(5), 6.10(6), 9.45(4) $\text{cm}^{-1}/\text{GPa}$, respectively. The L mode splits into two modes

282 (L', L'') and the $\partial v_i / \partial P$ values decrease from 8.05(31) to 5.09(9) and 7.37(7) $\text{cm}^{-1}/\text{GPa}$,
283 respectively. The v_4 mode becomes two peaks (v'_4, v''_4) with the $\partial v_i / \partial P$ from 2.48(9)
284 $\text{cm}^{-1}/\text{GPa}$ changing into 0.81(5) and 3.01(7) $\text{cm}^{-1}/\text{GPa}$, respectively. No split was
285 observed in mode v_1 but the pressure coefficient decreases obviously from 5.71(2) to
286 2.04(3) $\text{cm}^{-1}/\text{GPa}$ (Table 2).

287 The evolution and the pressure dependence of the Raman modes of $\text{BaMg}(\text{CO}_3)_2$
288 and $\text{BaMn}(\text{CO}_3)_2$ were showed in Figures S2-S5. From Raman spectra and shifts at
289 high pressure, similar structural phase transitions can be also observed in
290 $\text{BaMg}(\text{CO}_3)_2$ and $\text{BaMn}(\text{CO}_3)_2$ at 2.2-2.6 GPa and 3.7-4.1 GPa, respectively. These
291 results are comparable to the previous works of high-pressure XRD and Raman
292 experiments. Pippinger et al. (2014) reported that a structural transition occurred from
293 an $R\bar{3}m$ to $C2/c$ structure at approximately 2.32 GPa in $\text{BaMg}(\text{CO}_3)_2$ by the single-
294 crystal XRD experiment. Liang et al. (2019) found a similar structural phase transition
295 may occur in $\text{BaMn}(\text{CO}_3)_2$ between 3.0 and 3.8 GPa by Raman scattering
296 measurement. The slight difference of phase transition pressures may be attributed to
297 the uncertainty of different detecting methods. When the pressures reach 2.6 and 4.1
298 GPa for the $\text{BaMg}(\text{CO}_3)_2$ and $\text{BaMn}(\text{CO}_3)_2$, respectively, the T and L modes undergo
299 various degrees of splitting, with the values of the slope $\partial v_i / \partial P$ for each Raman
300 vibration changing drastically. Meanwhile, the v_4 mode splits into two new modes,
301 and the slope $\partial v_i / \partial P$ of v_1 mode exhibits an obvious decrease. The v_2 mode of
302 norsethite also shows a discontinuous change. The detailed pressure coefficients of
303 $\text{BaMg}(\text{CO}_3)_2$, and $\text{BaMn}(\text{CO}_3)_2$ are listed in Tables S1 and S2, respectively.
304 Reversibility of the phase transition of the norsethite-type minerals from α -phase to γ -
305 phase has been confirmed by the consistency between decompressed spectra and
306 initial spectra. In addition, the similar phase transition seems complete faster in

307 BaMg(CO₃)₂ and BaMn(CO₃)₂ than in BaFe(CO₃)₂, with no two-phase coexistence
308 observed in the former two.

309 We calculate the isothermal mode Grüneisen γ_{iT} to further understand the
310 elasticity properties of the norsethite-type minerals at high pressure, which is
311 calculated as follows (Gillet et al. 1989):

$$312 \quad \gamma_{iT} = \frac{K_T}{v_{i0}} \left(\frac{\partial v_i}{\partial P} \right)_T \quad (3)$$

313 where v_{i0} and $\partial v_i / \partial P$ are the frequencies fitted linearly by $v_i = v_{i0} + (\partial v_i / \partial P) \times P$, v_{i0} is
314 the frequency of mode v_i at 0 GPa, and P is pressure. K_T is the bulk modulus with
315 values of 40.3(7) and 91.2(24) GPa for α - and γ -BaFe(CO₃)₂ (this study), and 66.2(23)
316 and 41.9(4) GPa for α - and γ -BaMg(CO₃)₂, respectively (Pippinger et al. 2014). The
317 results are listed in Tables 2 and S1. The average γ_{iT} values of CO₃ group (0.17 for
318 BaMg(CO₃)₂, 0.18 for BaFe(CO₃)₂) are much smaller than that of the external lattice
319 modes (1.685 for BaMg(CO₃)₂, 1.095 for BaFe(CO₃)₂) in low-pressure phase. In γ -
320 phase, the difference of compressibility gets larger with a smaller γ_{iT} value of CO₃
321 group (0.06 for BaMg(CO₃)₂, 0.22 for BaFe(CO₃)₂) and a larger γ_{iT} value of the
322 external lattice vibrations (2.09 for BaMg(CO₃)₂, 3.81 for BaFe(CO₃)₂). γ_{iT} values are
323 small for the C-O bonds, which reflects their relative incompressibility and weak
324 expansivity. Hence, the weaker bonds, corresponding to the external lattice modes at
325 low frequency, are more affected by increasing pressure. The change in volume is
326 mainly caused by the weaker bonds. It is obvious that the carbonate groups in
327 BaMg(CO₃)₂ and BaFe(CO₃)₂ are much more incompressible than cation octahedra,
328 which is consistent with other carbonates (e.g., MgCO₃ from Liang et al. 2018).

329

330

Implications

331 Cationic substitution is an important factor to affect the evolution and stability of
332 crystal structure, phase transition pressure, the positions and frequency shifts of
333 spectroscopic peaks for different carbonate structures. The phase transition pressures
334 of BaMg(CO₃)₂, BaFe(CO₃)₂, and BaMn(CO₃)₂ are 2.4(2), 2.7(5), and 3.9(2) GPa in
335 this study, respectively. Compared with this study and previous results (Lin et al.
336 2012; Spivak et al. 2014; Cerantola et al. 2015; Merlini et al. 2015; Palaich et al.
337 2015; Fu et al. 2017; Merlini et al. 2017; Vennari and Williams 2018; Binck et al.
338 2020; Chariton et al. 2020; Wang et al. 2022), the phase stability of norsethite-type
339 Ba(Mg,Fe,Mn)(CO₃)₂, dolomite-type Ca(Mg,Fe,Mn)(CO₃)₂, and calcite-type
340 (Mg,Fe,Mn)CO₃ carbonates at ambient temperature were presented in Figure 7. The
341 effective cation radii of Ba²⁺, Ca²⁺, Mn²⁺, Fe²⁺, and Mg²⁺ are 1.35, 1.00, 0.83, 0.78,
342 and 0.72 Å at ambient conditions, respectively (Shannon and Prewitt 1969). With the
343 addition of the norsethite-type members, it is more clear that a smaller metal cation
344 tends to stabilize the trigonal structure to higher pressure (Wang et al. 2022), and the
345 phase transition pressures are much lower for norsethite-type carbonates than that of
346 calcite- and dolomite-type carbonates. A cation octahedron with a smaller cation has
347 shorter bonds and smaller compressibility, it thus can delay the polyhedral tilting and
348 distortion at high pressure (Ross and Reeder 1992; Santillán and Williams 2004;
349 Pippinger et al. 2014). However, different from the linear trend reported previously
350 (Wang et al. 2015), the relationship tends to be nonlinear in the norsethite-type
351 minerals join. Taking a closer look at the effects of ionic radii on the phase transition
352 of different carbonate structures, the substitution of Mg²⁺, Fe²⁺, and Mn²⁺ could
353 change the kinetic barriers of phase transition by changing the effective cation radii.
354 The onset phase transition pressures to high-pressure phases increase with cations
355 radii for norsethite-type minerals, while the results are opposite for both calcite- and

356 dolomite-type carbonates. We attributed this to the structure difference. In particular,
357 the norsethite-type carbonates are composed of octahedral (Mg,Fe,Mn)O₆, trigonal
358 planar (CO₃)²⁻, and polyhedra BaO₁₂ groups (Liang et al. 2019), while the dolomite-
359 type carbonates are composed by alternation layers of octahedral (Mg,Fe,Mn)O₆,
360 (CO₃)²⁻, and octahedral CaO₆ groups (Binck et al. 2020). The ionic radii display a
361 significant difference between (Mg, Fe, Mn)²⁺ (0.72-0.83 Å) and Ba²⁺ (1.35 Å) in
362 norsethite-type carbonates, while the values of (Mg, Fe, Mn)²⁺ are close to Ca²⁺ (1.00
363 Å) in dolomite-type carbonates. Although the atomic distribution of the norsethite-
364 type carbonates is topologically related to that of the dolomite-type minerals, the
365 larger ratio between the radii of the Ba²⁺/(Mg²⁺, Mn²⁺, Fe²⁺) ions compared to that of
366 Ca²⁺/(Mg²⁺, Mn²⁺, Fe²⁺) causes a distinct rotation of the carbonate group around
367 (0001) plane (Liang et al. 2019). The difference in structure may lead to the change of
368 high-pressure phase transition mechanism of cation (Mg²⁺, Mn²⁺, Fe²⁺) substitution.
369 These results provide new insights into the divalent cation substitution effects on the
370 stability and structural evolution of carbonates under high-pressure conditions.

371 The effect of ionic radii on phase transition pressures have been found not only in
372 carbonate minerals, but also in other materials, such as rare-earth vanadates (Gong et
373 al. 2018), gallium-bearing sphalerite-structure compounds (Zhang et al. 2021), and
374 lead-free niobate ceramics (Yan et al. 2019). Consistent with the results in this study,
375 the substance with a smaller ionic radius has a higher structural stability in
376 isostructural materials. Once the relationship between the ionic radius and the phase
377 transition pressure in a crystal structure is confirmed, the high-pressure structural
378 stability of isostructural materials might be predicted. Moreover, the ionic radius can
379 be added as the optimization variables to improve the high-pressure properties of the
380 resistant materials (Yan et al. 2019), which may provide a possible way for high-

381 pressure material synthesis and design.

382

383

Acknowledgments

384 We appreciate two anonymous reviewers for their constructive suggestions and
385 comments, which helped improve the manuscript significantly. We thank Wen Liang
386 for providing the norsethite samples and guidance on the experiments. We
387 acknowledge Dawei Fan, Zhilin Ye and Shijie Huang for the *in situ* X-ray diffraction
388 measurements. We are also grateful to the support of beamline scientists at BL15U1
389 of SSRF. This study was supported by the Strategic Priority Research Program (B) of
390 the Chinese Academy of Sciences (XDB 18010401), the Chinese Academy of
391 Sciences “Light of West China” Program (2019), and the National Natural Science
392 Foundation of China (NSFC grant no. 42104101).

393

394 **References**

- 395 Angel, R.J., Gonzales-Platas, J., and Alvaro, M. (2014) EosFit7c and a fortran module
396 (library) for equation of state calculations. *Zeitschrift für Kristallographie*, 229,
397 405-419.
- 398 Binck, J., Chariton, S., Stekiel, M., Bayarjargal, L., Morgenroth, W., Milman, V.,
399 Dubrovinsky, L., and Winkler, B. (2020) High-pressure, high-temperature phase
400 stability of iron-poor dolomite and the structures of dolomite-IIIc and dolomite-
401 V. *Physics of the Earth and Planetary Interiors*, 299, 106403.
- 402 Birch, F. (1947) Finite elastic strain of cubic crystals. *Physical Review*, 71, 809-924.
- 403 Böttcher, M.E., Gehlken, P.L., Skogby, H., and Reutel, C. (1997) The vibrational
404 spectra of BaMg(CO₃)₂ (norsethite). *Mineralogical Magazine*, 61, 249-256.
- 405 Böttcher, M.E. (2000) Stable isotope fractionation during experimental formation of
406 Norsethite (BaMg[CO₃]₂): A Mineral Analog of Dolomite. *Aquatic*
407 *Geochemistry*, 6, 201-213.
- 408 Böttcher, M.E., Effenberger, H.S., Gehlken, P.L., Grathoff, G.H., Schmidt, B.C.,
409 Geprägs, P., Bahlo, R., Dellwig, O., Leipe, T., Winde, V., Deutschmann, A.,
410 Stark, A., Gallego-Torres, D., and Martinez-Ruiz, F. (2012) BaMn[CO₃]₂ - a
411 previously unrecognized double carbonate in low-temperature environments:
412 structural, spectroscopic, and textural tools for future identification. *Chemie der*
413 *Erde*, 72, 85-89.
- 414 Böttcher, M. E., Gehlken, P. L., and Liang, W. (2022). The mid-infrared spectrum of
415 a new double carbonate, BaFe[CO₃]₂. *Journal of Molecular Structure*, 1250, 3-7.

- 416 Cerantola, V., McCammon, C., Kuppenko, I., Kantor, I., Marini, C., Wilke, M.,
417 Ismailova, L., Solopova, N., Chumakov, A., and Pascarelli, S. (2015) High-
418 pressure spectroscopic study of siderite (FeCO_3) with a focus on spin crossover.
419 American Mineralogist, 100, 2670-2681.
- 420 Chariton, S., McCammon, C., Vasiukov, D.M., Stekiel, M., Kantor, A., Cerantola, V.,
421 Kuppenko, I., Fedotenko, T., Koemets, E., and Hanfland, M. (2020) Seismic
422 detectability of carbonates in the deep Earth: A nuclear inelastic scattering study.
423 American Mineralogist, 105, 325-332.
- 424 Costanzo, A., Moore, K.R., Wall, F., and Feely, M. (2006) Fluid inclusions in apatite
425 from Jacupiranga calcite carbonatites: Evidence for a fluid-stratified carbonatite
426 magma chamber. Lithos, 91(1-4), 208-228.
- 427 Dong, X.C., Yue, J.L., Wang, E.Q., Li, M.L., and Li, G.Y. (2015) Microstructure and
428 superhardness effect of VC/TiC superlattice films. Transactions of Nonferrous
429 Metals Society of China (English Edition), 25(8), 2581-2586.
- 430 Effenberger, H., and Zemann, J. (1985) Single crystal X-ray investigation of
431 norsethite, $\text{BaMg}(\text{CO}_3)_2$: one more mineral with an aplanar carbonate group.
432 Zeitschrift für Kristallographie, 171, 275-280.
- 433 Effenberger, H., Pippinger, T., Libowitzky, E., Lengauer, C.L., and Miletich, R.
434 (2014) Synthetic norsethite, $\text{BaMg}(\text{CO}_3)_2$: revised crystal structure, thermal
435 behavior and displacive phase transition. Mineralogical Magazine, 78 (7), 1589-
436 1611.
- 437 Efthimiopoulos, I., Germer, M., Jahn, S., Harms, M., Reichmann, H.J., Speziale, S.,

- 438 Schade, U., Sieber, M., and Koch-Müller, M. (2019) Effects of hydrostaticity on
439 the structural stability of carbonates at lower mantle pressures: the case study of
440 dolomite. *High Pressure Research*, 39(1), 36-49.
- 441 Efthimiopoulos, I., Jahn, S., Kuras, A., Schade, U., and Koch-Müller, M. (2017)
442 Combined high-pressure and high-temperature vibrational studies of dolomite:
443 phase diagram and evidence of a new distorted modification. *Physics and
444 Chemistry of Minerals*, 44(7), 465-476.
- 445 Farsang, S., Facq, S., and Redfern, S.A.T. (2018) Raman modes of carbonate minerals
446 as pressure and temperature gauges up to 6 GPa and 500 °C. *American
447 Mineralogist*, 103(12), 1988-1998.
- 448 Fu, S., Yang, J., and Lin, J.F. (2017) Abnormal Elasticity of Single-Crystal
449 Magnesiosiderite across the Spin Transition in Earth's Lower Mantle. *Physical
450 Review Letters*, 118(3), 1-6.
- 451 Gabitov, R.I., Sadekov, A., Dyer, J., Perez-Huerta, A., Xu, H., and Migdisov, A.
452 (2021) Sectoral and growth rate control on elemental uptake by individual calcite
453 crystals. *Chemical Geology*, 585(August), 120589.
- 454 Gong, J., Fan, X., Dai, R., Wang, Z., Ding, Z., and Zhang, Z. (2018) High-Pressure
455 Phase Transition of Micro- and Nanoscale HoVO_4 and High-Pressure Phase
456 Diagram of REVO_4 with RE Ionic Radius [Research-article]. *ACS Omega*,
457 3(12), 18227 - 18233.
- 458 Gillet, P., Guyot, F., and Malezieux, J.M. (1989) High-pressure, high-temperature
459 Raman spectroscopy of Ca_2GeO_4 (olivine form): some insights on

- 460 anharmonicity. *Physics of the Earth and Planetary Interiors*, 58, 141-154.
- 461 Gillet, P., Biellmann, C., Reynard, B., and McMillan, P. (1993) Raman spectroscopic
462 studies of carbonates part I: high-pressure and high-temperature behavior of
463 Calcite, Magnesite, Dolomite and Aragonite. *Physics and Chemistry of Minerals*,
464 20(1), 1-18.
- 465 Gunasekaran, S., Anbalagan, G., and Pandi, S. (2006) Raman and infrared spectra of
466 carbonates of calcite structure. *Journal of Raman Spectroscopy*, 37(9), 892-899.
- 467 Hammersley, A.P., Svensson, S.O., Hanfland, M., Fitch, A.N., and Hausermann, D.
468 (1996) Two-dimensional detector software: From real detector to idealised image
469 or two-theta scan. *High Pressure Research*, 14, 235-248.
- 470 Helmersson, U., Todorova, S., Barnett, S.A., Sundgren, J.E., Markert, L.C., and
471 Greene, J.E. (1987) Growth of single-crystal TiN/VN strained-layer superlattices
472 with extremely high mechanical hardness. *Journal of Applied Physics*, 62(2),
473 481-484.
- 474 Hood, W.C., Steidl, P.F., and Tschopp, D.G. (1974) Precipitation of norsethite at
475 room temperature. *American Mineralogist*, 59(5-6), 471-474.
- 476 Klotz, S., Chervin, J.C., Munsch, P., and Le Marchand, G. (2009) Hydrostatic limits
477 of 11 pressure transmitting media. *Journal of Physics D: Applied Physics*, 42(7).
- 478 Larson, A.C., and Von Dreele, R.B. (2000) GSAS general structure analysis system
479 operation manual. Los Alamos Natl Lab LAUR 86-748:1-179.
- 480 Le Bail, A., Duroy, H., and Fourquet, J.L. (1988) Ab initio structure determination of
481 LiSbWO_6 by X-ray powder diffraction. *Mater Res Bull* 23:447-452.

- 482 Liang, W., Li, L., Yin, Y., Li, R., Li, Z., Liu, X., Zhao, C., Yang, S., Meng, Y., Li, Z.,
483 He, Y., and Li, H. (2019) Crystal structure of norsethite-type $\text{BaMn}(\text{CO}_3)_2$ and
484 its pressure-induced transition investigated by Raman spectroscopy. *Physics and*
485 *Chemistry of Minerals*, 46, 771-781.
- 486 Liang, W., Peters, C., Li, L., Leupold, O., Li, H., and Böttcher, M.E. (2021)
487 $\text{BaFe}[\text{CO}_3]_2$, a new double carbonate: Synthesis, structural characterization, and
488 geostability implications for high and low PT. *Geochemistry*, 81(2), 125740.
- 489 Lin, J.F., Liu, J., Jacobs, C., and Prakapenka, V.B. (2012). Vibrational and elastic
490 properties of ferromagnesite across the electronic spin-pairing transition of iron.
491 *American Mineralogist*, 97(4), 583-591.
- 492 Lindner, M., Saldi, G.D., Jordan, G., and Schott, J. (2017) On the effect of aqueous
493 barium on magnesite growth - A new route for the precipitation of the ordered
494 anhydrous Mg-bearing double carbonate norsethite. *Chemical Geology*, 460, 93-
495 105.
- 496 Lindner, M., Saldi, G.D., Carrocci, S., Bénézech, P., Schott, J., and Jordan, G. (2018)
497 On the growth of anhydrous Mg-bearing carbonates - Implications from
498 norsethite growth kinetics. *Geochimica et Cosmochimica Acta*, 238, 424-437.
- 499 Lippmann, F. (1967) Die kristallstruktur des norsethith, $\text{BaMg}(\text{CO}_3)_2$. *Mineralogy and*
500 *Petrology*, 12, 299-318.
- 501 Lippmann, F. (1973) *Sedimentary Carbonate Minerals*. Springer, Berlin.
- 502 Liu, C., and Li, W. (2020) Transformation of amorphous precursor to crystalline
503 carbonate: Insights from Mg isotopes in the dolomite-analogue mineral

- 504 norsethite [BaMg(CO₃)₂]. *Geochimica et Cosmochimica Acta*, 272, 1-20.
- 505 Liu, J., Caracas, R., Fan, D., Bobocioiu, E., Zhang, D., and Mao, W.L. (2016) High-
506 pressure compressibility and vibrational properties of (Ca,Mn)CO₃. *American*
507 *Mineralogist*, 101(12), 2723-2730.
- 508 Maeda, F., Ohtani, E., Kamada, S., Sakamaki, T., Hirao, N., and Ohishi, Y. (2017)
509 Diamond formation in the deep lower mantle: a high-pressure reaction of
510 MgCO₃ and SiO₂. *Scientific Reports*, 7, 40602.
- 511 Mao, H.K., Xu, J., and Bell, P.M. (1986) Calibration of the ruby pressure gauge to
512 800 kbar under quasi-hydrostatic conditions. *Journal of Geophysical Research*,
513 91(B5), 4673.
- 514 Mao, Z., Armentrout, M., Rainey, E., Manning, C.E., Dera, P., Prakapenka, V.B., and
515 Kavner, A. (2011) Dolomite III: A new candidate lower mantle carbonate.
516 *Geophysical Research Letters*, 38(22), 2-5.
- 517 Merlini, M., Crichton, W.A., Hanfland, M., Gemmi, M., Müller, H., Kuppenko, I., and
518 Dubrovinsky, L. (2012) Structures of dolomite at ultrahigh pressure and their
519 influence on the deep carbon cycle. *Proceedings of the National Academy of*
520 *Sciences of the United States of America*, 109(34), 13509-13514.
- 521 Merlini, M., Hanfland, M., and Gemmi, M. (2015) The MnCO₃-II high-pressure
522 polymorph of rhodocrosite. *American Mineralogist*, 100(11-12), 2625-2629.
- 523 Merlini, M., Cerantola, V., Gatta, G.D., Gemmi, M., Hanfland, M., Kuppenko, I., Lotti,
524 P., Müller, H., and Zhang, L. (2017) Dolomite-IV: Candidate structure for a
525 carbonate in the Earth's lower mantle. *American Mineralogist*, 102(8), 1763-

- 526 1766.
- 527 Ming, X., Wang, X.L., Du, F., Yin, J.W., Wang, C.Z., and Chen, G. (2011) First-
528 principles study of pressure-induced magnetic transition in siderite FeCO₃.
529 Journal of Alloys and Compounds, 510(1), L1-L4.
- 530 Palaich, S.E.M., Heffern, R.A., Watenphul, A., Knight, J., and Kavner, A. (2015).
531 High-pressure compressibility and phase stability of Mn-dolomite (kutnohorite).
532 American Mineralogist, 100(10), 2242-2245.
- 533 Pimentel, C., and Pina, C.M. (2014) The formation of the dolomite-analog norsethite:
534 Reaction pathway and cation ordering. Geochimica et Cosmochimica Acta
535 142(1), 217-223.
- 536 Pimentel, C., and Pina, C.M. (2016) Reaction pathways toward the formation of
537 dolomite-analogs at ambient conditions. Geochimica et Cosmochimica Acta,
538 178, 259-267.
- 539 Pippinger, T., Miletich, R., Effenberger, H., Hofer, G., Lotti, P., and Merlini, M.
540 (2014) High-pressure polymorphism and structural transitions of norsethite,
541 BaMg(CO₃)₂. Physics and Chemistry of Minerals, 41, 737-755.
- 542 Reeder, R.J., and Dollase, W.A. (1989) Structural variation in the dolomite-ankerite
543 solid-solution series: An X-ray, Mössbauer, and TEM study. American
544 Mineralogist, 74, 1159-1167.
- 545 Rividi, N., Van, Z. M., Philippot, P., Ménez, B., Godard, G., and Poidatz, E. (2010).
546 Calibration of carbonate composition using micro-raman analysis: application to
547 planetary surface exploration. Astrobiology, 10(3), 293-309.

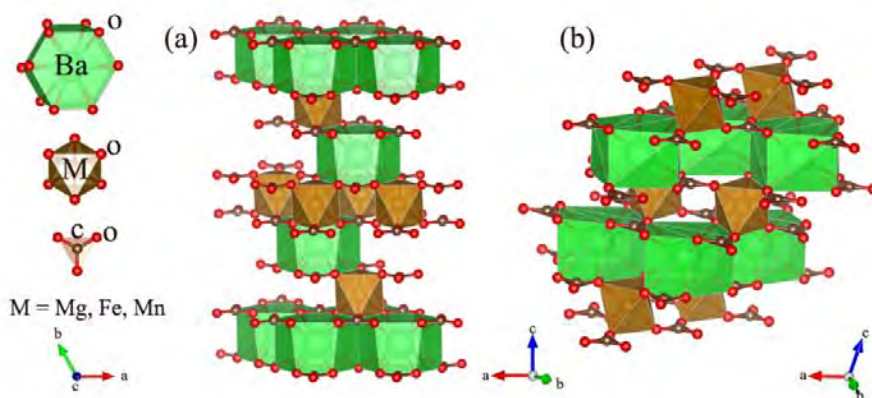
- 548 Ross, N.L., and Reeder, R.J. (1992) High-pressure structural study of dolomite and
549 ankerite. *American Mineralogist*, 77(3-4), 412-421.
- 550 Santillán, J., and Williams, Q. (2004) A high-pressure infrared and X-ray study of
551 FeCO_3 and MnCO_3 : Comparison with $\text{CaMg}(\text{CO}_3)_2$ -dolomite. *Physics of the*
552 *Earth and Planetary Interiors*, 143(1-2), 291-304.
- 553 Scheetz, B.E., and White, W.B. (1977) Vibrational spectra of the alkaline earth
554 double carbonates. *American Mineralogist*, 62, 36-50.
- 555 Schmidt, B.C., Gehlken, P.L., and Böttcher, M.E. (2013) Vibrational spectra of
556 $\text{BaMn}(\text{CO}_3)_2$ and a reanalysis of the Raman spectrum of $\text{BaMg}(\text{CO}_3)_2$. *European*
557 *Journal of Mineralogy*, 25, 137-144.
- 558 Shannon, R.D., and Prewitt, C.T. (1969) Effective ionic radii in oxides and fluorides.
559 *Acta Crystallographica*, B25, 925-946.
- 560 Shen, G., Wang, Y., Dewaele, A., Wu, C., Fratanduono, D.E., Eggert, J., Klotz, S.,
561 Dziubek, K.F., Loubeyre, P., Fat'yanov, O.V., Asimow, P.D., Mashimo, T., and
562 Wentzcovitch, R.M.M. (2020) Toward an international practical pressure scale:
563 A proposal for an IPPS ruby gauge (IPPS-Ruby2020). *High Pressure Research*,
564 40(3), 299-314.
- 565 Spivak, A., Solopova, N., Cerantola, V., Bykova, E., Zakharchenko, E., Dubrovinsky,
566 L., Litvin, Y. (2014) Raman study of MgCO_3 - FeCO_3 carbonate solid solution at
567 high pressures up to 55 GPa. *Physics and Chemistry of Minerals*, 41, 633-638.
- 568 Vennari, C.E., and Williams, Q. (2018) A novel carbon bonding environment in deep
569 mantle high-pressure dolomite. *American Mineralogist*, 103(1), 171-174.

- 570 Wang, F., Zhao, C., Xu, L., and Liu, J. (2022). Effects of hydrostaticity and Mn-
571 substitution on dolomite stability at high pressure. *American Mineralogist*, 89.
- 572 Wang, M., Liu, Q., Nie, S., Li, B., Wu, Y., Gao, J., Wei, X., and Wu, X. (2015) High-
573 pressure phase transitions and compressibilities of aragonite-structure
574 carbonates: SrCO₃ and BaCO₃. *Physics and Chemistry of Minerals*, 42(6), 517-
575 527.
- 576 Yan, K., Wang, F., Chen, X., Wu, D., and Zhu, K. (2019) Effects of A-site ionic size
577 on the phase transition behavior of lead-free niobate ceramics. *Ceramics*
578 *International*, 45(16), 20323-20330.
- 579 Zhang, X., Dai, L., Hu, H., and Hong, M. (2021) Pressure-induced metallic phase
580 transition in gallium arsenide up to 24.3 GPa under hydrostatic conditions.
581 *Modern Physics Letters B*, 35(28), 1-12.
- 582 Zhao, C., Xu, L., Gui, W., and Liu, J. (2020). Phase stability and vibrational
583 properties of iron-bearing carbonates at high pressure. *Minerals*, 10(12), 1-14.
- 584 Zhuravlev, Y.N., and Atuchin, V.V. (2020) Comprehensive density functional theory
585 studies of vibrational spectra of carbonates. *Nanomaterials*, 10(11), 1-19.
- 586 Zidarov, N., Petrov, O., Tarassov, M., Damyanov, Z., Tarassova, E., Petkova, V.,
587 Kalvachev, Y., and Zlatev, Z. (2009) Mn-rich norsethite from the Kremikovtsi
588 ore deposit, Bulgaria. *Neues Jahrbuch fur Mineralogie Abhandlungen*, 186, 321-
589 331.
- 590
- 591
- 592

593

594

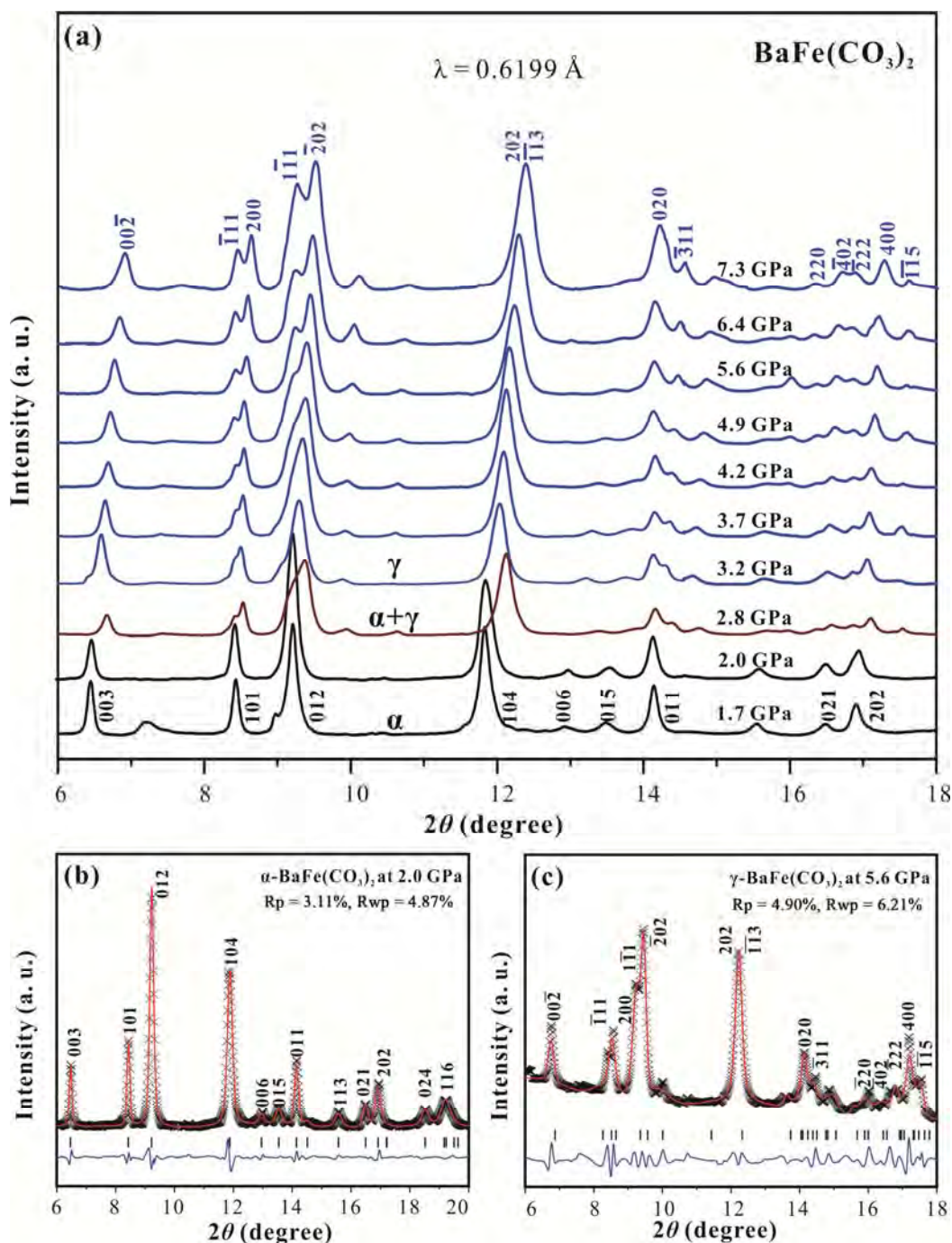
595 **Figure Captions**



596

597 **Figure 1.** Crystal structures of α -BaFe(CO₃)₂ (a) and γ -BaFe(CO₃)₂ phase (b).

598



599

600 **Figure 2.** High-pressure XRD patterns of BaFe(CO₃)₂ (a), representative XRD

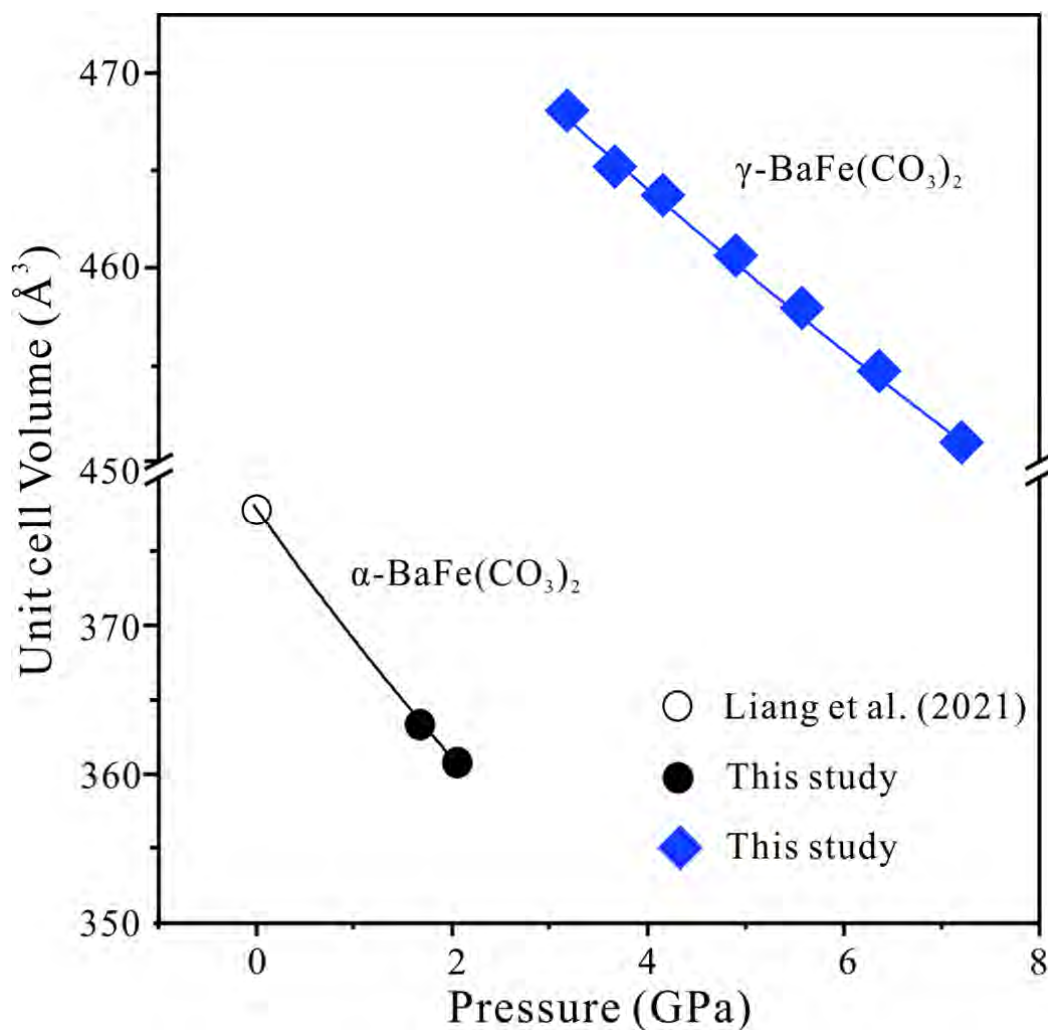
601 patterns of α-BaFe(CO₃)₂ phase at 2.0 GPa and 300 K (b), and γ-BaFe(CO₃)₂ phase at

602 5.6 GPa and 300 K (c). The black, red, and blue solid lines represent the α-, α + γ-

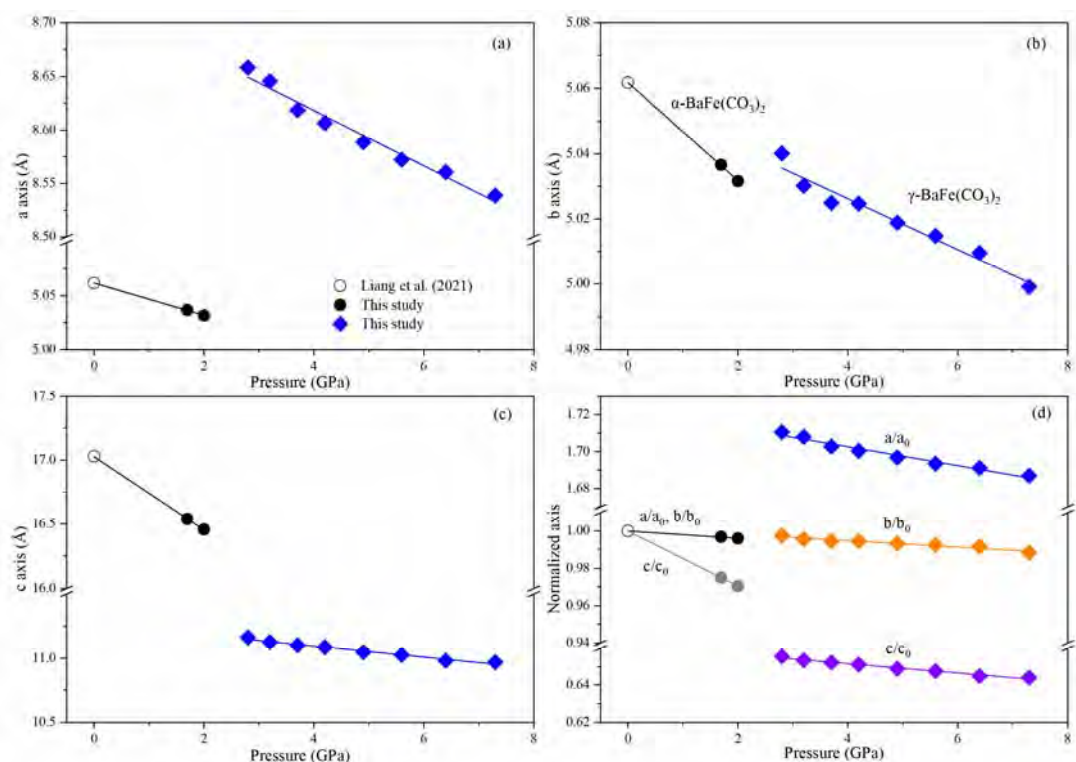
603 (coexistence of α-BaFe(CO₃)₂ and γ-BaFe(CO₃)₂ phase), and γ-BaFe(CO₃)₂. Le Bail

604 profile fits of the structural model of BaFe(CO₃)₂ with: α-phase (*R* $\bar{3}m$) at 0–2 GPa and

605 γ -phase ($C2/c$) at 3.2–7.3 GPa GPa. The black forks, red solid lines, and blue lines
606 stand for the observed, calculated, and deviation diffraction patterns, respectively. The
607 short black lines are the standardized diffraction peak positions of α - and γ -
608 $\text{BaFe}(\text{CO}_3)_2$ phase, respectively.



609
610 **Figure 3.** Pressure-volume profiles of $\text{BaFe}(\text{CO}_3)_2$. The black solid circles: α -
611 $\text{BaFe}(\text{CO}_3)_2$ phase, this study; blue solid diamonds: γ - $\text{BaFe}(\text{CO}_3)_2$, this study; black
612 open circle: α - $\text{BaFe}(\text{CO}_3)_2$ phase, Liang et al. (2021). The black and blue solid curves:
613 the BM2-EoS fit of α - $\text{BaFe}(\text{CO}_3)_2$ and γ - $\text{BaFe}(\text{CO}_3)_2$, respectively. Error bars smaller
614 than symbols are not shown for clarity.



616

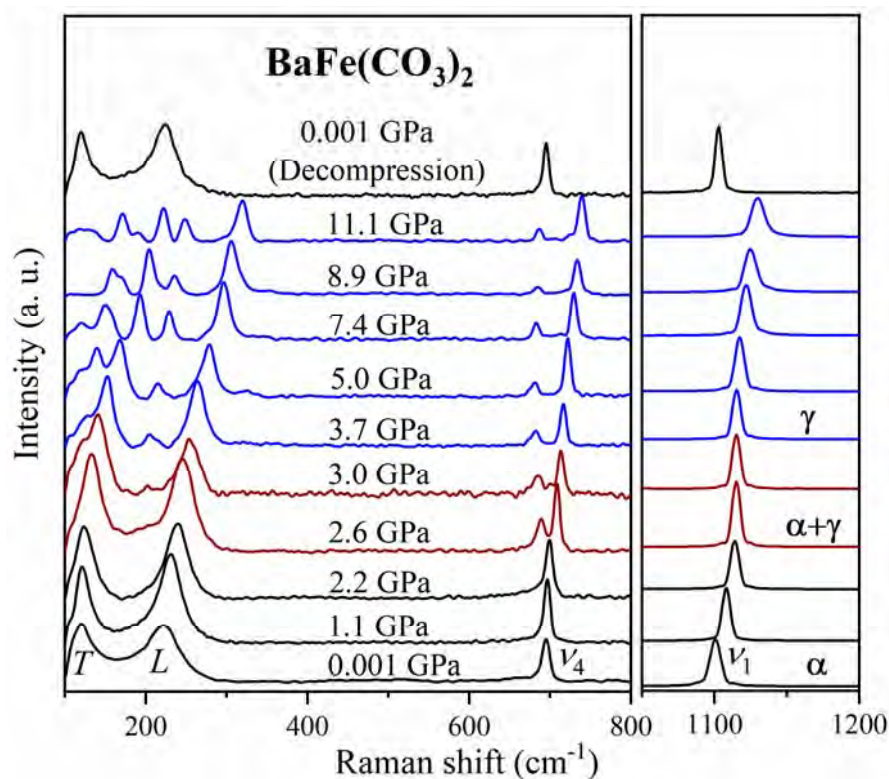
617 **Figure 4.** Second-order Birch–Murnaghan fittings to the compression pressure-lattice

618 parameters (a–c) and normalized lattice parameters (d) of BaFe(CO₃)₂. The black,

619 blue, orange and violet solid curves represent the BM2-EoS fittings of lattice

620 parameters. Error bars smaller than symbols are not shown for clarity.

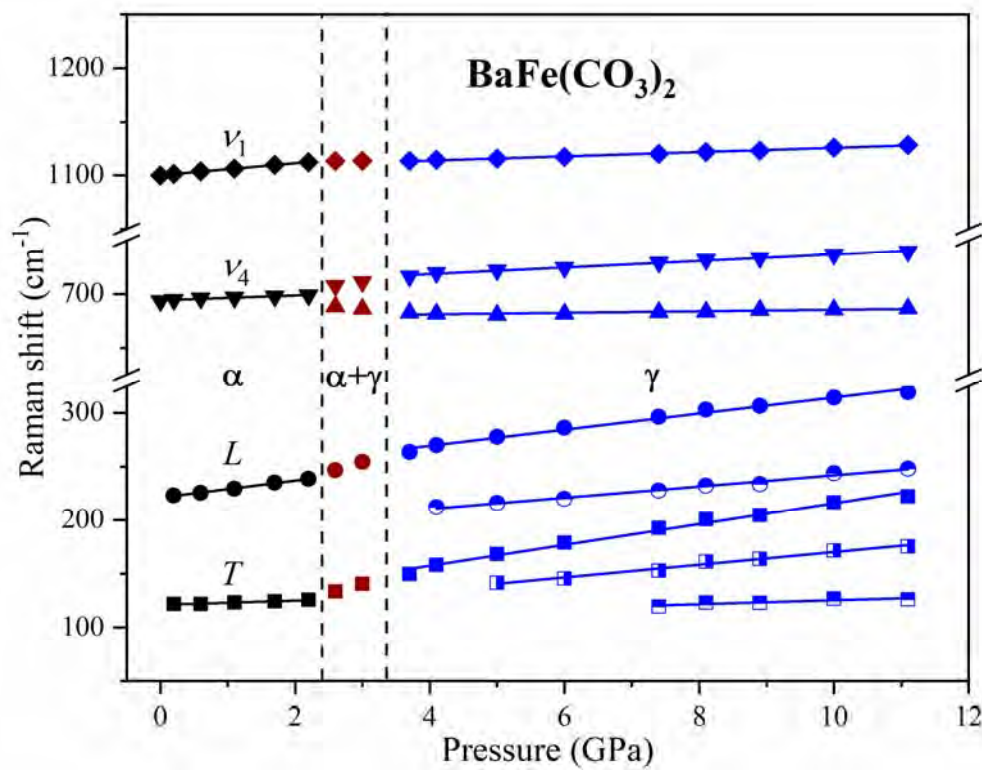
621



622

623 **Figure 5.** Representative Raman spectra of BaFe(CO₃)₂ at high pressures and room
624 temperature. The black, red, and blue solid lines represent the α-, α + γ- (coexistence
625 of α-BaFe(CO₃)₂ and γ-BaFe(CO₃)₂ phase), and γ-BaFe(CO₃)₂. The Raman spectrum
626 of recovered sample (after decompression from 11.1 GPa) is consistent with that of α-
627 BaFe(CO₃)₂ phase at ambient conditions, which indicates a reversible phase transition
628 of BaFe(CO₃)₂.

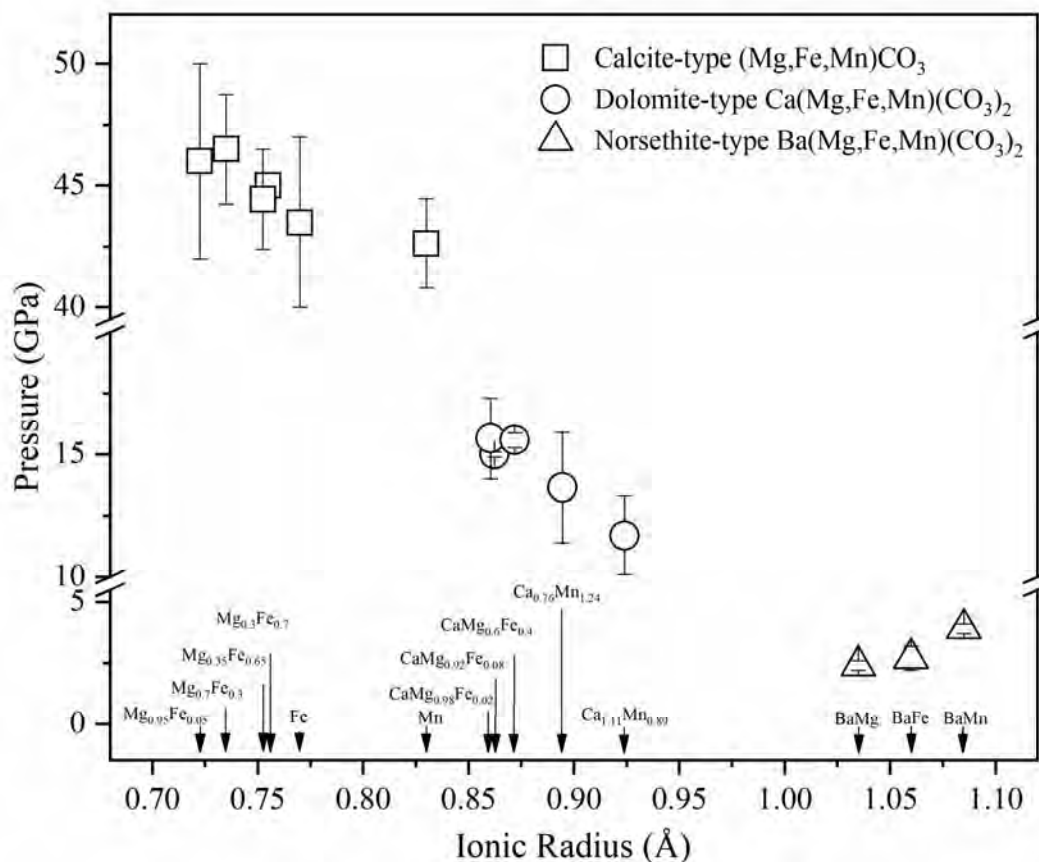
629



630

631 **Figure 6.** Representative Raman shifts of $\text{BaFe}(\text{CO}_3)_2$ at high pressures and room
632 temperature. Error bars smaller than symbols are not shown for clarity.

633



634

635 **Figure 7.** Phase stability of calcite-type $(\text{Mg,Fe,Mn})\text{CO}_3$, dolomite-type
 636 $\text{Ca}(\text{Mg,Fe,Mn})(\text{CO}_3)_2$, norsethite-type $\text{Ba}(\text{Mg,Fe,Mn})(\text{CO}_3)_2$ carbonates at ambient
 637 temperature. The data are derived from this study for $\text{BaMg}(\text{CO}_3)_2$, $\text{BaMn}(\text{CO}_3)_2$,
 638 $\text{BaFe}(\text{CO}_3)_2$, for $\text{Mg}_{0.95}\text{Fe}_{0.05}\text{CO}_3$ from Spivak et al. 2014, for $\text{Mg}_{0.7}\text{Fe}_{0.3}\text{CO}_3$ from
 639 Chariton et al. 2020, for $\text{Mg}_{0.35}\text{Fe}_{0.65}\text{CO}_3$ from Fu et al. 2017, for $\text{Mg}_{0.3}\text{Fe}_{0.7}\text{CO}_3$ from
 640 Lin et al. 2012, for FeCO_3 from Cerantola et al. 2015, for MnCO_3 from Merlini et al.
 641 2015, for $\text{CaMg}_{0.98}\text{Fe}_{0.02}(\text{CO}_3)_2$ from Binck et al. 2020, for $\text{CaMg}_{0.92}\text{Fe}_{0.08}(\text{CO}_3)_2$ from
 642 Vennari and Williams 2018, for $\text{CaMg}_{0.6}\text{Fe}_{0.4}(\text{CO}_3)_2$ from Merlini et al. 2017, for
 643 $\text{Ca}_{0.76}\text{Mn}_{1.24}(\text{CO}_3)_2$ from Palaich et al. 2015, and for $\text{Ca}_{1.11}\text{Mn}_{0.89}(\text{CO}_3)_2$ from Wang et
 644 al. 2022. The cation radii of Ba^{2+} , Ca^{2+} , Mn^{2+} , Fe^{2+} , and Mg^{2+} are 1.35, 1.00, 0.83,
 645 0.78, and 0.72 Å, respectively (Shannon and Prewitt 1969).

646

647 **Table 1.** Lattice constants and unit cell volumes of the α -BaFe(CO₃)₂ and γ -
648 BaFe(CO₃)₂ phase at high pressure and 300 K.

Phase	P (GPa)	<i>a</i> (Å)	<i>b</i> (Å)	<i>c</i> (Å)	β (°)	<i>V</i> (Å ³)	ρ (g/cm ³)
	0 ^a	5.062(1)	5.062(1)	17.027 (1)	-	377.79 (2)	3.34 (1)
α -phase (<i>R</i> $\bar{3}m$)	1.7	5.037 (1)	5.037 (1)	16.540 (1)	-	363.34 (18)	3.47 (2)
	2.0	5.032 (2)	5.032 (2)	16.456 (1)	-	360.79 (09)	3.50 (1)
	3.2	8.646 (2)	5.030 (1)	11.127 (3)	104.742 (2)	467.97 (12)	3.59 (4)
	3.7	8.619 (2)	5.025 (2)	11.104 (3)	104.751 (2)	465.06 (14)	3.61 (6)
	4.2	8.607 (2)	5.025 (2)	11.087 (3)	104.791 (2)	463.57 (13)	3.63 (1)
γ -phase (<i>C</i> 2/ <i>c</i>)	4.9	8.589 (2)	5.019 (2)	11.048 (3)	104.852 (2)	460.33 (14)	3.65 (4)
	5.6	8.572 (3)	5.015 (3)	11.027 (3)	105.023 (3)	457.83 (15)	3.67 (3)
	6.4	8.561 (3)	5.010 (3)	10.981 (3)	105.151 (3)	454.55 (15)	3.70 (1)
	7.3	8.538 (3)	4.993 (3)	10.968 (3)	105.341 (3)	450.90 (14)	3.73 (1)

649 **Notes:** In α -phase, $\alpha = \beta = 90^\circ$, $\gamma = 120^\circ$. In γ -phase, $\alpha = \gamma = 90^\circ$. ^a: Liang et al. (2021).

650

651 **Table 2.** Vibrational parameters of BaFe(CO₃)₂ at high pressures and room
652 temperature.

Raman modes	α -BaFe(CO ₃) ₂ (0–2.2 GPa)			γ -BaFe(CO ₃) ₂ (3.7–11.1 GPa)		
	ν_{0i}	dv_i/dP	γ_i	ν_{0i}	dv_i/dP	γ_i
<i>T</i>	123	2.03(11)	0.68	107	1.89(5)	1.62
				111	6.10(6)	5.08
				118	9.45(4)	7.12
<i>L</i>	221	8.05(31)	1.51	189	5.09(9)	2.44
				239	7.37(7)	2.79
ν_4	694	2.48(9)	0.15	678	0.81(5)	0.11
				706	3.01(7)	0.39
ν_1	1100	5.71 (2)	0.21	1106	2.04(3)	0.17

653 **Notes:** ν_{0i} are in cm⁻¹, dv_i/dP are in cm⁻¹/GPa. The reference frequency at room pressure (ν_{i0}) and pressure
654 coefficients, $\partial\nu_i/\partial P$, were used to calculate the mode Grüneisen parameters (γ_i) using the fitted K_{T0} values obtained
655 in this study from BM2-EoS fitting: $K_0=41.15(8)$ GPa for α -BaFe(CO₃)₂, $K_0=91.4(19)$ GPa for γ -BaFe(CO₃)₂.

656

657